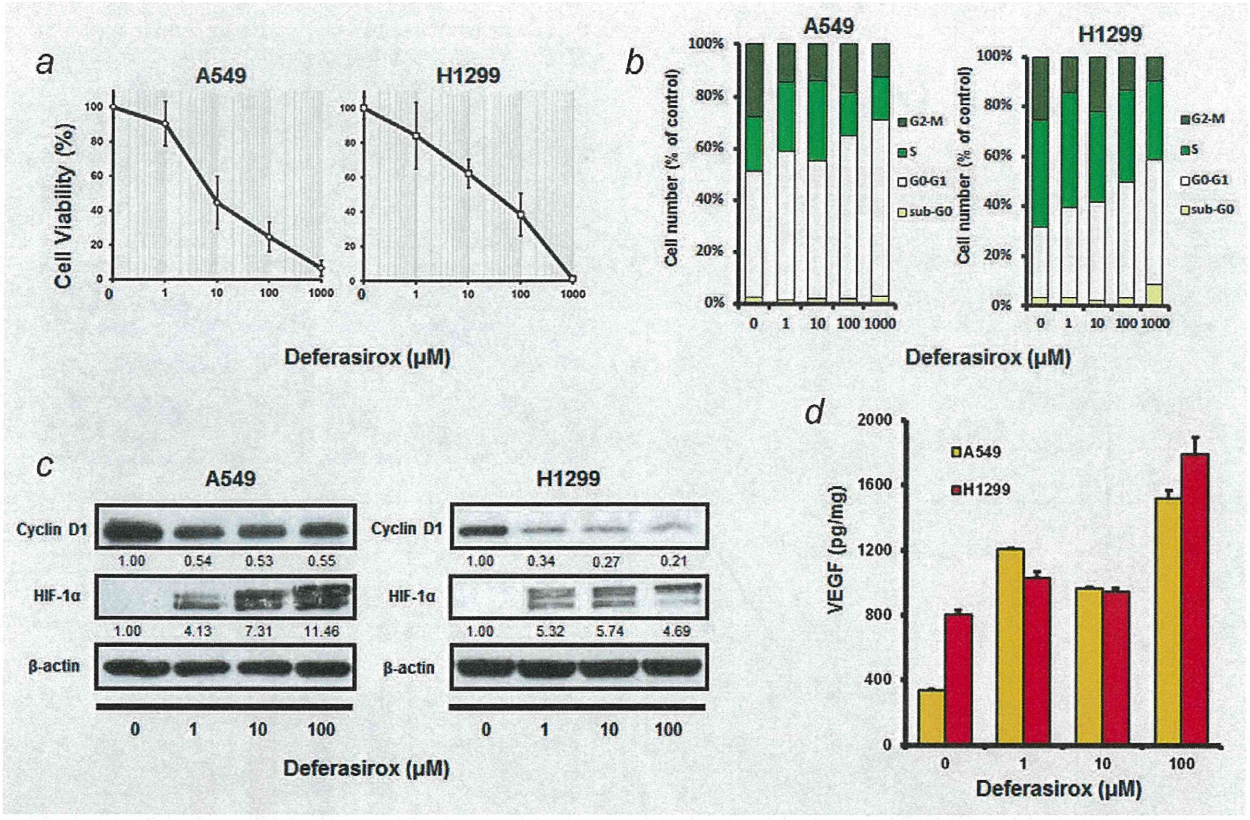

Figure 4. Iron depletion inhibited cell proliferation *via* cell-cycle arrest and induced VEGF secretion *in vitro*. (*a*) Cultured A549 cells and H1299 cells were treated with the indicated concentrations of deferasirox for 24 h and the cell viability was measured by the WST-1 method. (*b*) The cells were treated with different concentrations of deferasirox for 24 h and the cell-cycle distribution was analyzed by flow cytometry. Each histogram consists of the following four cell cycle populations; sub-G0 (black), G0-G1 (white), S (light gray) and G2-M (dark gray). (*c*) Whole-cell lysates and nuclear protein of these cells treated with the indicated concentrations of deferasirox were used for Western blot to determine its inhibitory effects on cell cycle and upregulation effects on HIF-1α. The expression level of each protein was calculated relative to its expression in mock-treated cells, whose expression level was designated as 1. (*d*) Supernatant treated with the indicated concentrations of deferasirox was harvested and VEGF secretion examined by ELISA.

deficient diet + bevacizumab [18 ± 5.1]) (Fig. 3*d*). None of the mice died owing to drug-induced toxicity and no other significant adverse events were observed.

Iron depletion inhibited cell proliferation via cell-cycle arrest in vitro

To reproduce an iron-depleted condition *in vitro*, an iron chelator was used (deferasirox, Exjade™). Deferasirox suppressed cancer cell proliferation in A549 and H1299 cells in a dose-dependent manner (Fig. 4*a*). To identify the mechanism of inhibition, a flow cytometry analysis for cell-cycle distribution was performed (Fig. 4*b*). Deferasirox increased the population of the G0-G1 phase in the A549 and H1299 cell lines. To confirm the results of the flow cytometry analysis, Western blot analysis was performed using a total protein extraction of the A549 and H1299 cells. The Western blot showed that deferasirox decreased cyclin D1 in a dose-dependent manner (Fig. 4*c*). Taken together, these results suggest that iron depletion inhibited cancer cell proliferation *via* cell-cycle arrest *in vitro*.

Iron depletion induced VEGF secretion in A549 and H1299 supernatant via upregulation of HIF-1α

To investigate whether iron depletion induces angiogenesis *via* HIF-1α, a Western blot analysis and ELISA assay were performed. Deferasirox treatment induced nuclear HIF-1α expression (Fig. 4*c*) and significantly increased VEGF secretion from A549 and H1299 cells, both in a dose-dependent manner (Fig. 4*d*). These results suggested that iron deficiency induced angiogenesis *via* HIF-1α and VEGF signaling. However, *in vitro* angiogenesis assay (tube formation assay) did not show the increase by deferasirox administration (Supporting Information Fig. S3). The reason was that deferasirox did not affect HUVEC in proliferation and VEGF secretion in the absence of tumor cells *in vitro*. Thus, the combination

effect of iron depletion with antiangiogenenic therapy is prominent only *in vivo* with tumor cells.

Discussion

Cancer cells have the ability to survive under severe conditions. One of the mechanisms for survival under hypoxic conditions is the activation of VEGF signaling *via* HIF-1α.[23] This mechanism also allows cancer cells to, sometimes, be able to resist chemotherapy.[24,25] Therefore, the effectiveness of chemotherapy can be compromised or attenuated. These experiences indicate that chemotherapy could be more effective under conditions where cancer cells would have difficulty resisting. Antiangiogenic drugs, especially bevacizumab, are known to have an excellent antitumor effect in the clinic[3–5] and are commonly used concurrently with antitumor drugs. When multiple antitumor and antiangiogenic drugs are prescribed, the financial burden on the patient is increased.[26,27] Therefore, a new strategy that would enhance the effect of antiangiogenic therapy would be beneficial. As iron depletion is known to reduce serum hemoglobin and oxygen supply to tissue in humans,[10,11] we hypothesized that iron depletion with antiangiogenic therapy could have a novel therapeutic effect for the treatment of cancer. Moreover, iron-controlled treatment has some advantages such as having its own antitumor effect, being easily controllable in daily living, and being inexpensive.

First, we examined the effect of iron depletion on the mice and tumor growth. The iron-depleted mice revealed low serum levels of hemoglobin, iron, red blood cells and ferritin compared to the mice fed a normal diet. Tumor growth was suppressed in the iron-depleted mice. Tumor tissue was extracted and examined by histology and immunohistology. Iron deposits in the stroma of the tumors were reduced in the iron-depleted mice. This phenomenon suggested that the iron condition of the tumor influenced not only the cancer cell but also stroma cells. Pimonidazole (Hypoxyprobe-1 kit) and CD-31 staining showed that iron depletion induced hypoxia and angiogenesis. To confirm hypoxia in the tumor and analyze the differences in cell signaling, we further examined the expression of HIF-1α. HIF-1α was predictably upregulated in iron-depleted tumors at the protein level. Taken together, these results suggested that iron depletion suppressed tumor growth and reciprocally induced angiogenesis *via* hypoxia. To the best of our knowledge, there is no previous report of this reciprocal phenomenon.

We next investigated the mechanism of iron deficiency and reciprocally induced angiogenesis *in vitro*. We used an iron chelator (deferasirox) to stimulate iron depletion owing to its usefulness *in vitro* and the expectation to apply it clinically. Deferasirox is the first orally bioavailable iron chelator with an indication for the treatment of iron overload in transfusion-dependent anemias. Deferasirox is the most useful iron chelator in the clinical setting and has been reported to have an antiproliferative effect in leukemia and hepatoma cells.[28,29] In our study, deferasirox inhibited the cancer cell proliferation in lung cancer cell lines A549 and H1299. We also examined apoptosis using the tunnel assay and found no significant difference in the deferasirox treatment group (data not shown). An ELISA assay and Western blot analysis showed that deferasirox treatment significantly increased VEGF secretion *via* upregulation of HIF-1α. Similar to the *in vivo* results, our *in vitro* study showed that iron depletion inhibited cancer cell proliferation and reciprocally induced angiogenesis. These results may suggest that the cancer cells overexpressed VEGF to escape the iron-depleted condition.

We then hypothesized that iron depletion increased the antitumor effect of an antiangiogenic drug. Bevacizumab, an antibody against VEGF, is the most common antiangiogenic drug used clinically and is approved for the treatment of many kinds of cancer. Bevacizumab is usually used as a combination with other antitumor drug. The reason is that bevacizumab is targeting only VEGF instead of the cancer cell. This is the first study of bevacizumab combination therapy with controlled internal iron condition. Bevacizumab had a dramatic synergistic antitumor effect with iron depletion in our *in vivo* study, indicating an inexpensive method to enhance the effectiveness of chemotherapy. Additionally, these findings may lead to the changes in the daily diet recommendations for patients being treated with an antiangiogenic drug. Iron depletion condition induced antiproliferative effect and angiogenesis. As a result, bevacizumab inhibited angiogenesis and provided strong antitumor effect. Of course, the mechanism is not completely explained and further *in vivo* studies are necessary. For example, *in vivo* live imaging of the tumor growth as well as angiogenesis may be extremely useful.[30–34]

Bevacizumab is an established antiangiogenic drug with clinical benefits for many kinds of cancer.[35,36] However, there is no reliable biomarker or method by which curative effect can be predicted.[37,38] Our study showed that bevacizumab combined with iron depletion was very effective; therefore, we hypothesized that serum iron level could be a novel bevacizumab biomarker. We previously conducted a retrospective study to investigate the correlation between serum hemoglobin level and bevacizumab response rate in 34 patients with colorectal cancer in our facility assessed by RECIST criteria between September 2007 and July 2010.[39] Patient characteristics are summarized in Supporting Information Table 1. The response rate of the low-Hb patient group was higher than that of high-Hb group (41.2 *vs.* 17.6%). This result combined with the results of our present study suggests that a prospective study of bevacizumab with iron control therapy in patients with cancer is warranted.

Conclusions

In conclusion, iron depletion inhibited the cancer cell proliferation and reciprocally induced angiogenesis *in vitro* and *in*

vivo. Bevacizumab had a dramatic synergistic antitumor effect with iron depletion. Treatment to create an iron-depleted condition could induce a novel therapeutic effect with antiangiogenic drugs in the treatment of cancer.

Acknowledgements

The authors are grateful to Mr. Toru Tanida and Ms. Tae Yamanishi for their technical assistance and Dr. Oka and Dr. Miyazaki of Saiwaicho Hospital (Okayama, Japan) for useful discussions.

References

1. Kim KJ, Li B, Winer J, et al. Inhibition of vascular endothelial growth factor-induced angiogenesis suppresses tumour growth in vivo. *Nature* 1993;362:841–4.
2. Forsythe JA, Jiang BH, Iyer NV, et al. Activation of vascular endothelial growth factor gene transcription by hypoxia-inducible factor 1. *Mol Cell Biol* 1996;16:4604–13.
3. Hurwitz H, Fehrenbacher L, Novotny W, et al. Bevacizumab plus irinotecan, fluorouracil, and leucovorin for metastatic colorectal cancer. *N Engl J Med* 2004;350:2335–42.
4. Kabbinavar FF, Hambleton J, Mass RD, et al. Combined analysis of efficacy: the addition of bevacizumab to fluorouracil/leucovorin improves survival for patients with metastatic colorectal cancer. *J Clin Oncol* 2005;23: 3706–12.
5. Saltz LB, Clarke S, Diaz-Rubio E, et al. Bevacizumab in combination with oxaliplatin-based chemotherapy as first-line therapy in metastatic colorectal cancer: a randomized phase III study. *J Clin Oncol* 2008;26:2013–19.
6. Richmond HG. Induction of sarcoma in the rat by iron-dextran complex. *Br Med J* 1959;1:947–9.
7. Okada S, Hamazaki S, Toyokuni S, et al. Induction of mesothelioma by intraperitoneal injections of ferric saccharate in male Wistar rats. *Br J Cancer* 1989;60: 708–11.
8. Kato J, Miyanishi K, Kobune M, et al. Long-term phlebotomy with low-iron diet therapy lowers risk of development of hepatocellular carcinoma from chronic hepatitis C. *J Gastroenterol* 2007;42: 830–6.
9. Hann HW, Stahlhut MW, Blumberg BS. Iron nutrition and tumor growth: decreased tumor growth in iron-deficient mice. *Cancer Res* 1988; 48:4168–70.
10. Becker A, Stadler P, Lavey RS, et al. Severe anemia is associated with poor tumor oxygenation in head and neck squamous cell carcinomas. *Int J Radiat Oncol Biol Phys* 2000;46: 459–66.
11. Vaupel P, Mayer A, Briest S, et al. Oxygenation gain factor: a novel parameter characterizing the association between hemoglobin level and the oxygenation status of breast cancers. *Cancer Res* 2003;63:7634–7.
12. Shirakawa Y, Naomoto Y, Kimura M, et al. Topological analysis of p21WAF1/CIP1 expression in esophageal squamous dysplasia. *Clin Cancer Res* 2000;6:541–50.
13. Chang YS, Adnane J, Trail PA, et al. Sorafenib (BAY 43-9006) inhibits tumor growth and vascularization and induces tumor apoptosis and hypoxia in RCC xenograft models. *Cancer Chemother Pharmacol* 2007;59:561–74.
14. Schmeding M, Rademacher S, Boas-Knoop S, et al. rHuEPo reduces ischemia-reperfusion injury and improves survival after transplantation of fatty livers in rats. *Transplantation* 2010;89: 161–8.
15. Fei J, Hong A, Dobbins TA, et al. Prognostic significance of vascular endothelial growth factor in squamous cell carcinomas of the tonsil in relation to human papillomavirus status and epidermal growth factor receptor. *Ann Surg Oncol* 2009;16:2908–17.
16. Myoung H, Hong SD, Kim YY, et al. Evaluation of the anti-tumor and anti-angiogenic effect of paclitaxel and thalidomide on the xenotransplanted oral squamous cell carcinoma. *Cancer Lett* 2001;163:191–200.
17. Hashimoto Y, Watanabe Y, Shirakiya Y, et al. Establishment of biological and pharmacokinetic assays of telomerase-specific replication-selective adenovirus. *Cancer Sci.* 2008;99:385–90.
18. Ohara T, Takaoka M, Toyooka S, et al. Inhibition of mTOR by temsirolimus contributes to prolonged survival of mice with pleural dissemination of non-small-cell lung cancer cells. *Cancer Sci* 2011;102:1344–9.
19. Kohgo Y, Niitsu Y, Kondo H, et al. Serum transferrin receptor as a new index of erythropoiesis. *Blood* 1987;70:1955–8.
20. Ke Q, Costa M. Hypoxia-inducible factor-1 (HIF-1). *Mol Pharmacol* 2006;70:1469–80.
21. Schicher N, Paulitschke V, Swoboda A, et al. Erlotinib and bevacizumab have synergistic activity against melanoma. *Clin Cancer Res* 2009; 15:3495–3502.
22. Argov M, Kashi R, Peer D, et al. Treatment of resistant human colon cancer xenografts by a fluoxetine-doxorubicin combination enhances therapeutic responses comparable to an aggressive bevacizumab regimen. *Cancer Lett* 2009;274:118–25.
23. Shima DT, Deutsch U, D'Amore PA. Hypoxic induction of vascular endothelial growth factor (VEGF) in human epithelial cells is mediated by increases in mRNA stability. *FEBS Lett* 1995;370: 203–8.
24. Guminski AD, Harnett PR, deFazio A. Scientists and clinicians test their metal-back to the future with platinum compounds. *Lancet Oncol* 2002;3: 312–8.
25. Chang A. Chemotherapy, chemoresistance and the changing treatment landscape for NSCLC. *Lung Cancer* 2011;71:3–10.
26. Tappenden P, Jones R, Paisley S, et al. The cost-effectiveness of bevacizumab in the first-line treatment of metastatic colorectal cancer in England and Wales. *Eur J Cancer* 2007;43: 2487–94.
27. Montero AJ, Avancha K, Gluck S, et al. A cost-benefit analysis of bevacizumab in combination with paclitaxel in the first-line treatment of patients with metastatic breast cancer. *Breast Cancer Res Treat* 2012;132: 747–51.
28. Ohyashiki JH, Kobayashi C, Hamamura R, et al. The oral iron chelator deferasirox represses signaling through the mTOR in myeloid leukemia cells by enhancing expression of REDD1. *Cancer Sci* 2009;100:970–77.
29. Lescoat G, Chantrel-Groussard K, Pasdeloup N, et al. Antiproliferative and apoptotic effects in rat and human hepatoma cell cultures of the orally active iron chelator ICL670 compared to CP20: a possible relationship with polyamine metabolism. *Cell Prolif* 2007;40:755–67.
30. Hoffman, RM. Orthotopic metastatic mouse models for anticancer drug discovery and evaluation: a bridge to the clinic. *Invest New Drugs* 1999;17:343–59.
31. Hoffman, RM. The multiple uses of fluorescent proteins to visualize cancer in vivo. *Nat Rev Cancer* 2005;5:796–806.
32. Hoffman RM, Yang M. Color-coded fluorescence imaging of tumor-host interactions. *Nat Protoc* 2006;1:928–35.
33. Amoh Y, Yang M, Li L, et al. Nestin-linked green fluorescent protein transgenic nude mouse for imaging human tumor angiogenesis. *Cancer Res* 2005;65:5352–7.
34. Amoh Y, Li L, Tsuji K, et al. Dual-color imaging of nascent blood vessels vascularizing pancreatic cancer in an orthotopic model demonstrates antiangiogenesis efficacy of gemcitabine. *J Surg Res* 2006;132:164–9.
35. Shih T, Lindley C. Bevacizumab: an angiogenesis inhibitor for the treatment of solid malignancies. *Clin Ther* 2006;28:1779–1802.
36. Wheatley-Price P, Shepherd FA. Targeting angiogenesis in the treatment of lung cancer. *J Thorac Oncol* 2008;3:1173–84.
37. Jubb AM, Harris AL. Biomarkers to predict the clinical efficacy of bevacizumab in cancer. *Lancet Oncol* 2010;11:1172–83.
38. Mancuso A, Sternberg CN. Colorectal cancer and antiangiogenic therapy: what can be expected in clinical practice?*Crit Rev Oncol Hematol* 2005;55: 67–81.
39. Eisenhauer EA, Therasse P, Bogaerts J, et al. New response evaluation criteria in solid tumours: revised RECIST guideline (version 1.1). *Eur J Cancer* 2009;45:228–47.

Published OnlineFirst September 30, 2013; DOI: 10.1158/1078-0432.CCR-13-0742

Clinical Cancer Research

Cancer Therapy: Preclinical

A Genetically Engineered Oncolytic Adenovirus Decoys and Lethally Traps Quiescent Cancer Stem-like Cells in S/G_2/M Phases

Shuya Yano[1], Hiroshi Tazawa[2], Yuuri Hashimoto[1], Yasuhiro Shirakawa[1], Shinji Kuroda[1], Masahiko Nishizaki[1], Hiroyuki Kishimoto[1], Futoshi Uno[1], Takeshi Nagasaka[1], Yasuo Urata[3], Shunsuke Kagawa[1], Robert M. Hoffman[4,5], and Toshiyoshi Fujiwara[1]

Abstract

Purpose: Because chemoradiotherapy selectively targets proliferating cancer cells, quiescent cancer stem-like cells are resistant. Mobilization of the cell cycle in quiescent leukemia stem cells sensitizes them to cell death signals. However, it is unclear that mobilization of the cell cycle can eliminate quiescent cancer stem-like cells in solid cancers. Thus, we explored the use of a genetically-engineered telomerase-specific oncolytic adenovirus, OBP-301, to mobilize the cell cycle and kill quiescent cancer stem-like cells.

Experimental Design: We established $CD133^+$ cancer stem-like cells from human gastric cancer MKN45 and MKN7 cells. We investigated the efficacy of OBP-301 against quiescent cancer stem-like cells. We visualized the treatment dynamics of OBP-301 killing of quiescent cancer stem-like cells in dormant tumor spheres and xenografts using a fluorescent ubiquitination cell-cycle indicator (FUCCI).

Results: $CD133^+$ gastric cancer cells had stemness properties. OBP-301 efficiently killed $CD133^+$ cancer stem-like cells resistant to chemoradiotherapy. OBP-301 induced cell-cycle mobilization from G_0–G_1 to S/G_2/M phases and subsequent cell death in quiescent $CD133^+$ cancer stem-like cells by mobilizing cell-cycle–related proteins. FUCCI enabled visualization of quiescent $CD133^+$ cancer stem-like cells and proliferating $CD133^-$ non–cancer stem-like cells. Three-dimensional visualization of the cell-cycle behavior in tumor spheres showed that $CD133^+$ cancer stem-like cells maintained stemness by remaining in G_0–G_1 phase. We showed that OBP-301 mobilized quiescent cancer stem-like cells in tumor spheres and xenografts into S/G_2/M phases where they lost viability and cancer stem-like cell properties and became chemosensitive.

Conclusion: Oncolytic adenoviral infection is an effective mechanism of cancer cell killing in solid cancer and can be a new therapeutic paradigm to eliminate quiescent cancer stem-like cells. *Clin Cancer Res; 19(23); 6495–505. ©2013 AACR.*

Introduction

Current cytotoxic chemoradiotherapy selectively targets proliferating cancer cells. Quiescent or dormant cancer cells in contrast are often drug-resistant and are a major impediment to cancer therapy (1, 2). Cancer stem-like cells or tumor-initiating cells (3–5) maintain a quiescent or dormant state, which appears to contribute to their resistance to conventional therapies (6–8). Recently, several therapeutic strategies have targeted inhibition of the cancer stem-like cell quiescent state. For example, treatment with arsenic trioxide enhanced the sensitivity of leukemia stem cells (LSC) to cytosine arabinoside through inhibition of LCS quiescence (9). Acute myeloid leukemia stem cells can be induced to enter the cell cycle and apoptosis by treatment with granulocyte colony-stimulating factor (10). However, it is still unclear whether cancer stem-like cells in solid tumors can also be eliminated by inducing them to cycle.

Viruses can infect target cells, multiply, cause cell death, and release viral particles. These features enable the use of viruses as anticancer agents that induce specific tumor lysis (11, 12). Adenoviral E1A, in particular, has been shown to exert tumor-suppressive functions, including enhancement of chemoradiotherapy-induced apoptosis via inhibition of the cellular DNA repair machinery (13)

Authors' Affiliations: [1]Department of Gastroenterological Surgery, Okayama University Graduate School of Medicine, Dentistry and Pharmaceutical Sciences; [2]Center for innovative clinical medicine, Okayama University Hospital, Okayama; [3]Oncolys BioPharma, Inc., Tokyo, Japan; [4]Department of Surgery, University of California San Diego; and [5]AntiCancer, Inc., San Diego, California

Note: Supplementary data for this article are available at Clinical Cancer Research Online (http://clincancerres.aacrjournals.org/).

Corresponding Author: Toshiyoshi Fujiwara, Department of Gastroenterological Surgery, Okayama University Graduate School of Medicine, Dentistry, and Pharmaceutical Sciences, 2-5-1 Shikata-cho, Kita-ku, Okayama 700-8558, Japan. Phone: 81-86-235-7255; Fax: 81-86-221-8775; E-mail: toshi_f@md.okayama-u.ac.jp

doi: 10.1158/1078-0432.CCR-13-0742

Published OnlineFirst September 30, 2013; DOI: 10.1158/1078-0432.CCR-13-0742

Translational Relevance

Current chemotherapy and radiotherapy target proliferating cancer cells, while having little effect on dormant cancer cells. Cancer stem–like cells can maintain a quiescent or dormant state, which contributes largely to their resistance to conventional therapies. Recently, several therapeutic strategies have targeted inhibition of the quiescent state in leukemia stem cells. However, it is still unclear whether cancer stem–like cells in solid tumors can also be eliminated by inhibition of their dormant state. Here, we show that a telomerase-specific adenovirus, OBP-301, mobilizes quiescent cancer stem–like cells to cycle and lethally traps them into S-phase. Moreover, we showed by spatiotemporal treatment dynamics that OBP-301 decoyed quiescent cancer stem–like cells in tumor spheres and xenografts into an S-phase trap where they lost viability and cancer stem–like cell properties and become chemosensitive. Thus, our data demonstrated that cell-cycle mobilization and $S/G_2/M$ phase trapping induced by adenoviral infection is an effective mechanism of killing cancer stem–like cells in solid cancers.

and inhibition of cell proliferation via suppression of EGH receptor (EGFR; ref. 14) and HER-2 (15). It has been recently reported that an oncolytic adenovirus efficiently eradicates cancer stem–like cells as well as non–cancer stem–like cells in brain tumors, breast cancer, and esophageal cancer (16–18).

In the present study, we isolated $CD133^+$ subpopulations from radioresistant cells in human gastric cancer cell lines and characterized them as cancer stem–like cells. By using multicolor cell-cycle imaging that color codes the quiescent cancer stem–like cells and proliferating non–cancer stem–like cells, we showed by treatment dynamics that a genetically engineered telomerase-specific oncolytic adenovirus, OBP-301 (19, 20), eradicates dormant $CD133^+$ cancer stem–like cells via cell-cycle mobilization both in tumor spheres and in subcutaneous tumors.

Materials and Methods

Cell lines and radiation treatment

The human gastric cancer cell lines MKN45 and MKN7 were maintained according to the vendor's specifications (21). Radioresistant MKN45 and MKN7 cells were established by administration of radiation treatments using an X-ray generator (MBR-1505R; Hitachi Medical Co.).

Recombinant adenoviruses

The recombinant tumor-specific, replication-selective adenovirus vector OBP-301 (Telomelysin), in which the promoter element of the human telomerase reverse transcriptase (hTERT) gene drives the expression of E1A and E1B genes linked to an internal ribosome entry site, was previously constructed and characterized (19, 22).

Isolation of $CD133^+$ and $CD133^-$ cells by flow cytometry

After incubation with an anti-CD133/2(293C)-allophycocyanin antibody (Miltenyi Biotec), $CD133^+$ cells were sorted by flow cytometry using a FACSAria flow cytometer (Becton Dickinson). $CD133^+$ and $CD133^-$ cells were separated by flow cytometry just before each experiment to ensure that the purity of the $CD133^+$ population was greater than 70%, and the purity of $CD133^-$ cells was above 99%.

Cell viability assay

$CD133^+$ and $CD133^-$ cells (5×10^2 cells/well) in 96-well plates were treated with OBP-301, cisplatin, or radiation at the indicated doses. Cell viability was determined on day 5 after treatment using the Cell Proliferation Kit II (Roche Molecular) according to the manufacturer's protocol.

Establishment of MKN45 cells stably transfected with FUCCI vector plasmids

FUCCI (fluorescent ubiquitination-based cell-cycle indicator) (23) was used to visualize the cell-cycle phases. Plasmids, expressing mKO2-hCdt1 (GFP) or mAG-hGem (orange fluorescence protein), were obtained from the Medical & Biological Laboratory. Plasmids expressing mKO2-hCdt1 or mAG-hGem were transfected into radioresistant MKN45 cells using Lipofectamine LTX (Invitrogen).

Western blot analysis

The primary antibodies used were: mouse anti-CD133/1(W6B3C) monoclonal antibody (mAb; Miltenyi Biotec); rabbit anti-E2F1 polyclonal antibody (pAb) (Santa Cruz Biotechnology); mouse anti-Ad5 E1A mAb (BD Pharmingen); mouse anti-c-Myc pAb, rabbit anti-phospho-Akt mAb, rabbit anti-Akt mAb, mouse anti-p27 mAb (all from Cell Signaling Technology); mouse anti-p53 mAb, mouse anti-p21 mAb (both from CALBIOCHEM Merck4 Biosciences); and mouse anti-β-actin mAb (Sigma-Aldrich). Immunoreactive bands on the blots were visualized using enhanced chemiluminescence substrates (ECL Plus; GE Healthcare).

Subcutaneous MKN45 tumor xenograft model

To evaluate a tumorigenicity of $CD133^+$ and $CD133^-$ cells, purified $CD133^+$ and $CD133^-$ cells from radioresistant MKN45 were inoculated at a density of 1×10^5 cells/site on the right and left sides, respectively, of the flank of 5-week-old female NOD/SCID mice (Charles River Laboratories) or athymic nude mice (Charles River Laboratories). To evaluate the *in vivo* antitumor efficacy of OBP-301, cisplatin, or radiation, the radioresistant MKN45 cells were inoculated at a density of 5×10^6 cells/site into the flank of 5-week-old female athymic nude mice. OBP-301 [1×10^8 plaque-forming units (PFU)] was injected into the tumors. Cisplatin (4 mg/kg body weight) was intraperitoneally injected and ionizing radiation (2 Gy) was administered to tumors after protection of normal tissues. Mice were treated every 3 days for a total of three treatments.

Published OnlineFirst September 30, 2013; DOI: 10.1158/1078-0432.CCR-13-0742

Imaging of MKN45 cells expressing cell-cycle–dependent fluorescent proteins

Time lapse images of FUCCI-expressing CD133$^+$ and CD133$^-$ radioresistant MKN45 cells were acquired using a confocal laser scanning microscope (FV10i; Olympus). Cross-sections of FUCCI-expressing tumors were imaged using a confocal laser scanning microscope (FV-1000; Olympus).

Treatment of subcutaneous FUCCI-expressing MKN45 tumors

To evaluate the *in vivo* antitumor efficacy of OBP-301, cisplatin, paclitaxel, or their combination, the FUCCI-expressing MKN45 cells were inoculated at a density of 5×10^6 cells/site into the flank of 5-week-old female athymic nude mice (Charles River Laboratories). OBP-301 (1×10^8 PFU/tumor) was injected into the tumors. Cisplatin (4 mg/kg) and paclitaxel (5 mg/kg) were injected intraperitoneally. Mice were treated every 3 days for a total of 3 to 5 treatments.

Statistical analysis

Data are shown as means ± SD. For comparison between 2 groups, significant differences were determined using the Student *t* test. For comparison of more than 2 groups, statistical significance was determined with a one-way ANOVA followed by a Bonferroni multiple-group comparison test. $P < 0.05$ was considered significant.

Results

CD133$^+$ cells in human gastric cancer cells are cancer stem–like

Cancer stem–like cells are more resistant to radiotherapy than non–cancer stem–like cells (24–26). To enrich cancer stem–like subpopulations, we established radioresistant MKN45 and MKN7 human gastric cancer cells. Radioresistant MKN45 and MKN7 cells had a significantly higher percentage of CD133$^+$ cells than parental cells (Fig. 1A and Supplementary Fig. S1A). We hypothesized that CD133 in gastric cancer would identify cancer cells with stem-like properties, such as asymmetric cell division, *in vitro* proliferation, dormancy, sphere formation, and *in vivo* tumorigenicity (5, 6). To investigate the asymmetric division of CD133$^+$ cells, we determined whether CD133$^+$ cells produce both CD133$^+$ and CD133$^-$ cells. CD133$^+$ cells generated both CD133$^+$ and CD133$^-$ cells, whereas CD133$^-$ cells could not produce CD133$^+$ cells (Supplementary Fig. S2). We compared *in vitro* proliferation of CD133$^+$ and CD133$^-$ cells. CD133$^+$ cells produced larger colonies than CD133$^-$ cells (Fig. 1B and Supplementary Fig. S3). CD133$^+$ cells made significantly much more tumor spheres than CD133$^-$ cells (Fig. 1B). CD133$^+$ cells produced tumors in immunodeficient nude mice and NOD/SCID mice, whereas CD133$^-$ cells did not generate tumors in either nude on NOD/SCID mice (Supplementary Fig. S4 and Fig. 1B). Furthermore, CD133$^+$ cells in radioresistant MKN45 and MKN7 cells were significantly more resistant to 5-fluorouracil, cisplatin, paclitaxel, and radiation than CD133$^-$ cells (Fig. 1C and Supplementary Fig. S1B). These data indicate that CD133$^+$ cells are cancer stem–like.

Quiescent CD133$^+$ cancer stem–like cells and cycling CD133$^-$ non–cancer stem–like cells are independently visualized by fluorescent cell-cycle indicator technology

Sakaue-Sawano and colleagues have reported that the cell-cycle state in viable cells can be visualized using the FUCCI system (23). We established FUCCI-expressing CD133$^+$ or CD133$^-$ radioresistant MKN45 cells, in which cell nuclei in G_0–G_1, S, or G_2–M phases exhibit red, yellow, or green fluorescence, respectively. We compared the cell-cycle phase of FUCCI-expressing CD133$^+$ or CD133$^-$ cells. Time-lapse imaging showed that most of CD133$^+$ cells were quiescent in G_0–G_1 phase with red fluorescent nuclei compared with CD133$^-$ cells (Fig. 1D). Similar results were also observed in flow cytometric analysis of the cell cycle (Supplementary Fig. S5A and S5B). CD133$^+$ cells had similar proliferation rates as CD133$^-$ cells until 3 days after seeding. CD133$^+$ cells showed lower proliferation rates than CD133$^-$ cells 5 days after seeding (Fig. 1D). This result was consistent with the cell-cycle status of CD133$^+$ cells which had an increased percentage of cells in G_0–G_1 phase. Moreover, we examined cell-cycle–related protein (27) expression in CD133$^+$ and CD133$^-$ cells. CD133$^+$ cells showed higher expressions of p53, p21, and p27 proteins compared with CD133$^-$ cells (Supplementary Fig. S8), suggesting that these proteins are involved in the maintenance of quiescent cancer stem–like cells.

OBP-301 efficiently kills cancer stem–like cells and reduces cancer stem–like cell frequency via enhanced viral replication

To evaluate the efficacy of OBP-301 against CD133$^+$ cancer stem–like cells, we treated CD133$^+$ and CD133$^-$ cells from radioresistant MKN45 and MKN7 cells with OBP-301. OBP-301 similarly killed CD133$^+$ and CD133$^-$ cells (Fig. 2A and Supplementary Fig. S1B). Next we investigated whether OBP-301 could decrease cancer stem–like cell frequency. Flow cytometric analysis showed that OBP-301 significantly decreased the percentage of CD133$^+$ cells compared with cisplatin or radiation (Fig. 2A). Expression of *CD133* mRNA was closely associated with the population of CD133$^+$ cells (Supplementary Fig. S6). OBP-301 significantly suppressed the expression of *CD133* mRNA compared with cisplatin and radiation (Supplementary Fig. S7). Western blot analysis also showed that cisplatin and radiation, but not OBP-301, increased CD133 expression 3- to 5-fold in CD133$^+$ cells (Fig. 2D). Moreover, pretreatment of CD133$^+$ cells with OBP-301, but not cisplatin or radiation, significantly decreased the number of tumor spheres (Supplementary Fig. S13). These data indicated that OBP-301 kills both CD133$^+$ and CD133$^-$ cells and reduces cancer stem–like cell frequency.

To further explore the efficacy of OBP-301 against CD133$^+$ cancer stem–like cells, we assessed the relationship between hTERT activity and viral replication. OBP-301 contains the hTERT promoter, which allows it to tumor-specifically regulate the gene expression of E1A and E1B for viral replication (19). Quantitative reverse transcriptation

Published OnlineFirst September 30, 2013; DOI: 10.1158/1078-0432.CCR-13-0742

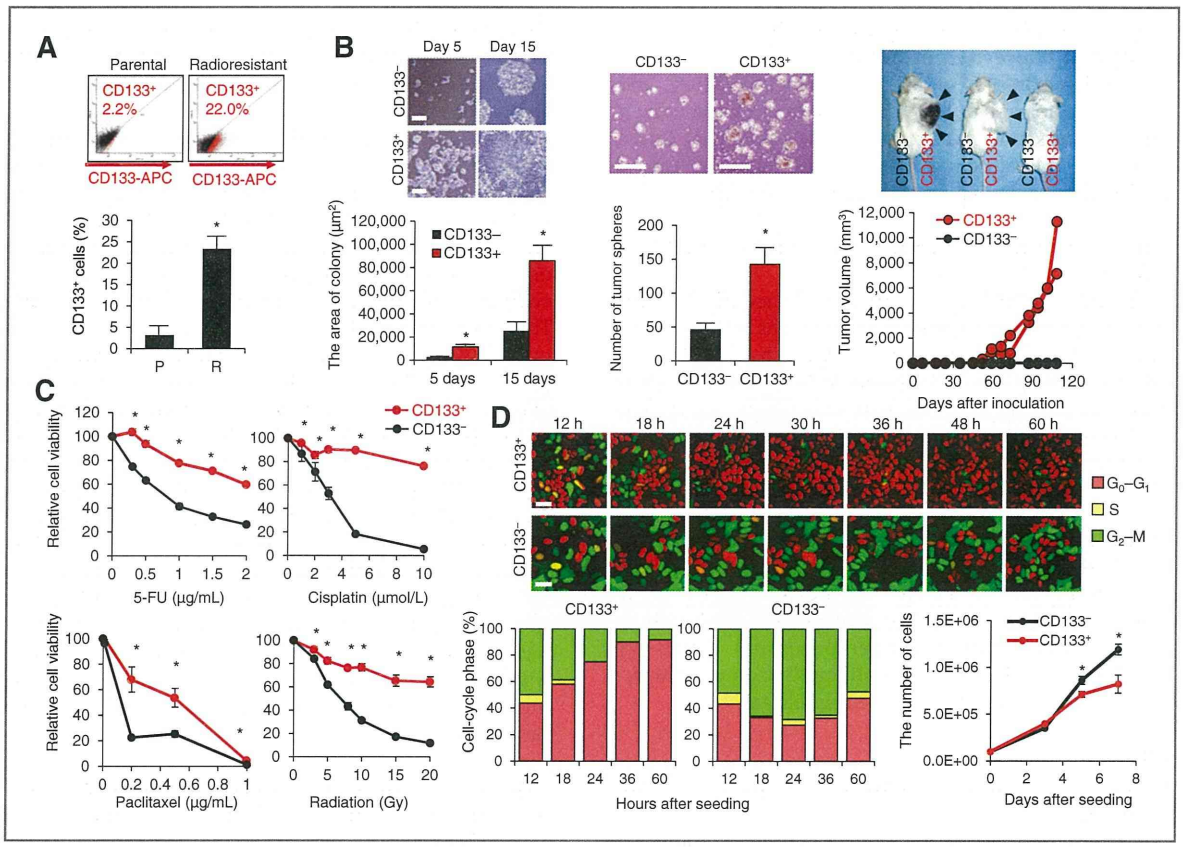

Figure 1. CD133$^+$ cancer stem–like cells in human gastric cancer exhibit cancer stem–like cell properties and are more quiescent. A, flow cytometric analysis of CD133 expression in parental (P) and radioresistant (R) MKN45 cells. Representative dot plots (top) and data from 5 experiments (bottom) are shown. B, CD133$^+$ MKN45 cancer cells exhibit cancer stem–like properties. Representative images of colonies from CD133$^+$ or CD133$^-$ cells. Histogram shows the size of colonies from CD133$^+$ or CD133$^-$ cells (left). Quantitative measurement of the tumor sphere–forming potential of CD133$^+$ and CD133$^-$ cells (middle). Representative images of tumor spheres derived from CD133$^+$ and CD133$^-$ cells. Histogram shows the numbers of tumor spheres from CD133$^+$ or CD133$^-$ cells. Scale bars, 500 μm. Tumorigenicity of CD133$^+$ and CD133$^-$ cells in immunodeficient NOD/SCID mice (right). Growth curve of each tumor and representative photographs are shown. C, sensitivity of CD133$^+$ and CD133$^-$ cells from radioresistant MKN45 cells to 5-fluorouracil, cisplatin, paclitaxel, and irradiation. D, time-lapse imaging of CD133$^+$ and CD133$^-$ cells from radioresistant MKN45 cells expressing cell-cycle–dependent fluorescent proteins (FUCCI; top). The cells in G_0–G_1, S, or G_2–M phases appear red, yellow, or green, respectively. Histogram shows the cell-cycle phase of FUCCI-expressing CD133$^+$ and CD133$^-$ cells cultured for 48 hours after sorting (bottom left). The percentage of cells in G_0–G_1, S, and G_2–M phases are shown. Cell proliferation rate of CD133$^+$ and CD133$^-$ cells (bottom right). Scale bars, 50 μm. Data are shown as means ± SD ($n = 5$). *, $P < 0.01$.

PCR (qRT-PCR) showed that CD133$^+$ cells had a significant, 3-fold higher expression of *hTERT* mRNA than CD133$^-$ cells (Fig. 2B), suggesting that CD133$^+$ cancer stem–like cells have a higher activity of hTERT than CD133$^-$ cells. Next we compared the expression of *E1A* mRNA and E1A protein in CD133$^+$ cells and in CD133$^-$ cells. qRT-PCR showed that the expression of *E1A* mRNA in CD133$^+$ cells was higher than that in CD133$^-$ cells (Fig. 2B). Western blotting showed that the expression of E1A in CD133$^+$ cells was higher than that in CD133$^-$ cells (Fig. 2B). Furthermore, we compared the copy number of the E1A gene, which is indicative of viral replication, in CD133$^+$ and CD133$^-$ cells after infection with OBP-301. As expected, the copy number of the E1A gene in CD133$^+$ cells was significantly higher than that in CD133$^-$ cells (Fig. 2B). These data indicate that OBP-301 is efficiently cytopathic for CD133$^+$ cells due to enhanced viral replication.

OBP-301 mobilizes and lethally traps quiescent cancer stem–like cells into S-phase in monolayer culture

To examine whether OBP-301 could change the cell-cycle phase of quiescent CD133$^+$ cells, we treated FUCCI-expressing CD133$^+$ cells with OBP-301. Time-lapse imaging showed that OBP-301 infection significantly decreased the percentage of CD133$^+$ cells in G_0–G_1 phase, increased the percentage of CD133$^+$ cells in S-phase, and killed them in S-phase (Fig. 2C and Supplementary Movie S1). Similar results were also observed in flow cytometric analysis of the cell cycle (Supplementary Fig. S5C and S5D). These results suggest that OBP-301 induces cell-cycle activation of quiescent CD133$^+$ cells from G_0–G_1 phase to S-phase and kills them. We next assessed the molecular mechanism by which OBP-301 induces mobilization of the cell cycle in quiescent cancer stem–like cells. OBP-301 increased the expression of E2F1, c-Myc, and phospho-Akt proteins that function as

Published OnlineFirst September 30, 2013; DOI: 10.1158/1078-0432.CCR-13-0742

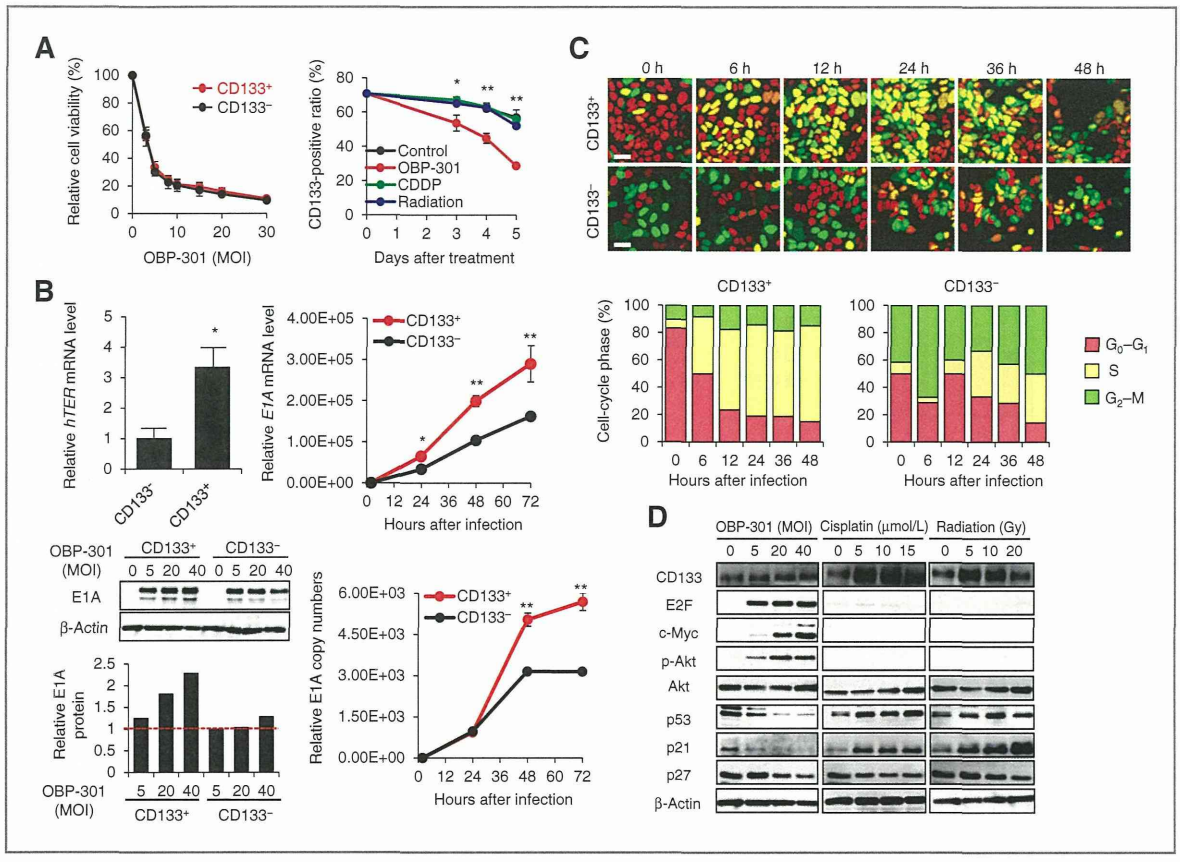

Figure 2. OBP-301 lethally induces S-phase transition of quiescent CD133$^+$ cancer stem–like cells and decreases cancer stem–like cell frequency via enhanced viral replication. A, OBP-301 efficiently kills CD133$^+$ cancer stem–like cells. Left, viability of CD133$^+$ and CD133$^-$ MKN45 cells after OBP-301 infection. Right, CD133-positive ratio of MKN45 cells treated with OBP-301, cisplatin, or radiation was analyzed by flow cytometry. B, OBP-301 can replicate more in CD133$^+$ cells that have more hTERT activity than in CD133$^-$ cells. Expression of *hTERT* mRNA in CD133$^+$ and CD133$^-$ MKN45 cells assessed by qRT-PCR (top left). The relative levels of *hTERT* mRNA were calculated after normalization with reference to the expression of *PBGD* mRNA. Expression of *E1A* mRNA in CD133$^+$ and CD133$^-$ MKN45 cells after OBP-301 infection at an MOI of 10 PFU/cell for 2 hours. Expression of *E1A* mRNA was analyzed over the following 3 days by qRT-PCR (top right). The relative levels of *E1A* mRNA were calculated after normalization with reference to the expression of *GAPDH* mRNA. Western blot analysis of E1A expression in CD133$^+$ and CD133$^-$ MKN45 cells treated with OBP-301 for 48 hours (bottom left). Quantitative relative expression level of E1A protein, normalized to β-actin, using NIH ImageJ software (bottom left). Quantitative measurement of viral DNA replication in CD133$^+$ and CD133$^-$ MKN45 cells after OBP-301 infection at an MOI of 10 PFU/cell for 2 hours (bottom right). *E1A* copy number was analyzed over the following 3 days using qPCR. C, time-lapse imaging of FUCCI-expressing CD133$^+$ and CD133$^-$ cells treated with OBP-301 at an MOI of 20 PFU/cell. The cells in G_0–G_1, S, or G_2–M phases appear red, yellow, or green, respectively. Histogram shows the cell-cycle phases of FUCCI-expressing CD133$^+$ and CD133$^-$ cells treated with OBP-301 for 48 hours. The percentage of cells in G_0–G_1, S, and G_2–M phases are shown. D, Western blot analysis of E2F1, c-Myc, phospho-Akt, Akt, p53, p21, and p27 expression in CD133$^+$ cells treated with OBP-301, cisplatin, or radiation for 48 hours. β-Actin was assayed as a loading control for all experiments. Data are shown as means ± SD ($n = 5$). *, $P < 0.05$; **, $P < 0.01$.

cell-cycle accelerators (27) and decreased the expression of p53, p21, and p27 proteins that function as cell-cycle brakes (27) in quiescent CD133$^+$ cells (Fig. 2D). In contrast, cisplatin and radiation increased the expression of p53 and p21 proteins (Fig. 2D). We further examined whether adenoviral E1A altered the expression of these proteins in CD133$^+$ cells. E1A-expressing OBP-301 and Ad5, but not E1A-defficient dl312, similarly altered the expression of these proteins in CD133$^+$ cells (Supplementary Fig. S9). These results indicate that OBP-301 induces cell-cycle progression through upregulation of E2F-related proteins and downregulation of p53-related and p27 proteins by enhanced adenoviral E1A in quiescent cancer stem–like cells.

Three-dimensional tumor spheres maintain a CD133$^+$ subpopulation by remaining quiescent

Formation of tumor spheres under serum-free conditions is frequently used to maintain cancer stem–like cell subpopulations (28). The addition of serum makes floating undifferentiated tumor spheres adherent and their cells differentiate into adherent cells (29). Therefore, we hypothesized that tumor spheres maintained their cancer stem–like cell frequency due to quiescence.

Published OnlineFirst September 30, 2013; DOI: 10.1158/1078-0432.CCR-13-0742

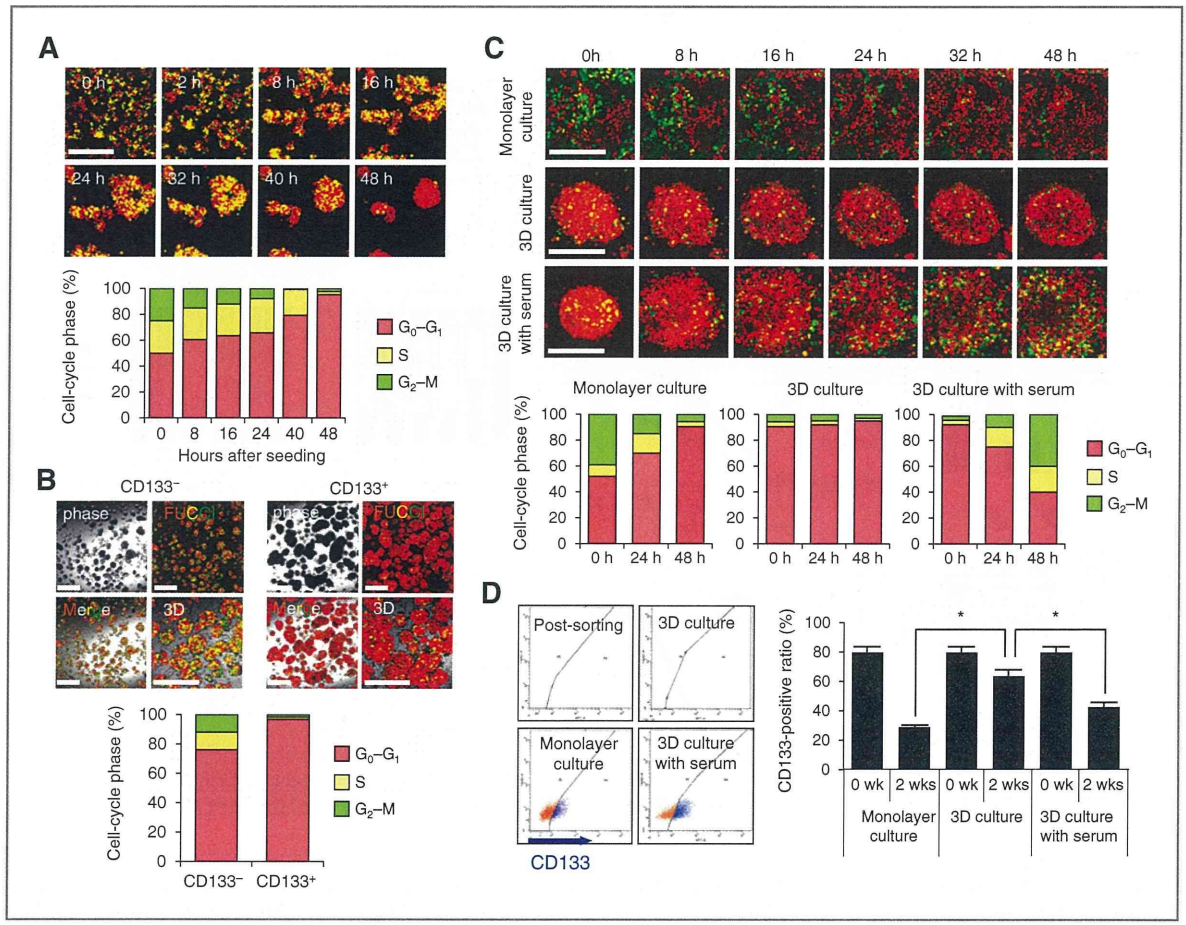

Figure 3. Three-dimensional tumor spheres maintain CD133$^+$ cells by the cell cycle arrest. A, time-lapse images of FUCCI-expressing CD133$^+$ cells in 3-dimensional culture without serum. Purified FUCCI-expressing CD133$^+$ cells were cultured on agar in serum-free medium containing EGF and bFGF for 48 hours (top). The cells in G_0–G_1, S, or G_2–M phases appear red, yellow, or green, respectively. Histogram shows the cell-cycle phase of FUCCI-expressing CD133$^+$ cells in 3-dimensional culture without serum (bottom). The percentage of cells in G_0–G_1, S, and G_2–M phases are shown. B, representative images of tumor spheres formed from FUCCI-expressing CD133$^+$ and CD133$^-$ cells (top). Histogram shows the cell-cycle phase of tumor spheres from FUCCI-expressing CD133$^+$ and CD133$^-$ cells (bottom). C, time-lapse images of FUCCI-expressing CD133$^+$ cells in monolayer culture or FUCCI-expressing tumor spheres in 3-dimensional culture without serum (3D without serum) or tumor spheres in monolayer culture with serum (monolayer culture; top). Histogram shows the cell-cycle phase of FUCCI-expressing CD133$^+$ cells in 2D culture, FUCCI-expressing established tumor spheres in 3D without serum, or tumor spheres on plastic culture with serum (monolayer culture; bottom). D, comparison of changes in the CD133$^+$-positive ratio in monolayer culture, tumor spheres in 3D culture without serum, or with serum. Representative dot plots (left) and data from 3 experiments (right) are shown. Data are shown as means ± SD ($n = 5$). *, $P < 0.01$. Scale bars, 500 μm.

CD133$^+$ cells aggregated and formed tumor spheres, and arrested in G_0–G_1 phase (Fig. 3A). Tumor spheres formed from CD133$^+$ cells contained more quiescent cells than those formed from CD133$^-$ cells (Fig. 3B). Moreover, established tumor spheres formed from CD133$^+$ cells remained quiescent in 3-dimensional culture without serum (Fig. 3C). In contrast, established tumor spheres, after addition of serum, exited from the quiescent state and began to cycle, divide, and increase (Fig. 3C and Supplementary Movie S2). Flow cytometric analysis showed that CD133$^+$ cells could be maintained in tumor spheres cultured in serum-free medium for 2 weeks, whereas the percentage of CD133$^+$ cells significantly decreased in monolayer cultures or in tumor spheres cultured in serum-containing medium (Fig. 3D). These data indicate that tumor spheres maintain their cancer stem-cell frequency by remaining dormant.

Real-time imaging spatiotemporally shows OBP-301 eliminates dormant tumor spheres by cell-cycle mobilization and S/G_2/M phase trapping

To further evaluate OBP-301-induced cell-cycle mobilization and S-phase trapping in dormant tumor spheres, we visualized the treatment dynamics of FUCCI-expressing tumor spheres infected with OBP-301. Time-lapse imaging showed that OBP-301 infected quiescent CD133$^+$ cells at the periphery of the spheres and then induced S and G_2–M

Published OnlineFirst September 30, 2013; DOI: 10.1158/1078-0432.CCR-13-0742

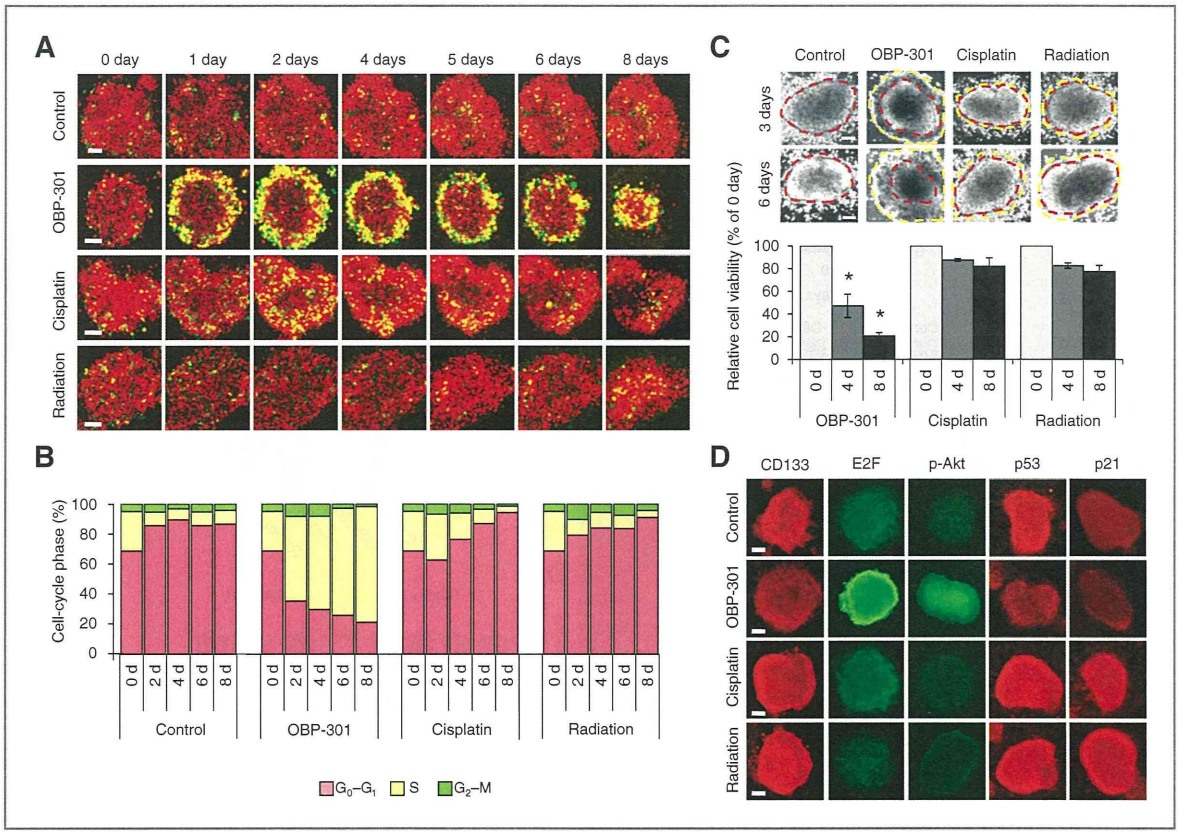

Figure 4. Visualization of elimination of dormant tumor spheres by virus infection. A, time-lapse images of tumor spheres treated with OBP-301 (5×10^6 PFU), cisplatin (10 μmol/L), or radiation (10 Gy). The cells in G_0–G_1, S, or G_2–M phases appear red, yellow, or green, respectively. B, histogram shows the cell-cycle phases of the spheres with OBP-301, cisplatin, or radiation. The percentage of cells in G_0–G_1, S, and G_2–M phases are shown. C, representative images of control, OBP-301-, cisplatin-, or radiation-treated spheres (top). Histogram shows the relative cell viability of treated tumor spheres (bottom). D, the $CD133^+$ tumor spheres treated as above were stained for E2F1, phospho-Akt, p53, and p21. Immuofluorescence staining was visualized by confocal laser microscopy. Scale bars, 100 μm. Data are shown as means ± SD ($n = 5$). *, $P < 0.01$.

phase entry, leading to cellular death by viral replication (Fig. 4A). Moreover, as OBP-301 penetrated into the deeper layers, tumor spheres gradually shrunk after virus infection (Fig. 4A and C). In contrast, cisplatin and radiation did not affect the cell-cycle phase or the size of tumor spheres (Figs. 4A–C and Supplementary Movie S3). Immunofluorescence staining of tumor spheres also confirmed that OBP-301 infection downregulated CD133, p53, and p21 expression and upregulated E2F1 and phospho-Akt expression in tumor spheres (Fig. 4D). These results suggest that OBP-301 efficiently eradicates dormant tumor spheres resistant to conventional therapies by mobilizing them into an $S/G_2/M$ phase trap.

OBP-301 efficiently kills dormant cancer stem–like cells in established human tumor xenografts by cell-cycle mobilization and $S/G_2/M$ phase trapping, thereby reducing cancer stem–like cell frequency

To further confirm whether OBP-301 efficiently reduced $CD133^+$ cancer stem–like cell frequency within tumor tissues (Supplementary Fig. S10A), we investigated the expression of *CD133* mRNA and the CD133-positive ratio in subcutaneous tumors derived from radioresistant MKN45 cells after treatment of OBP-301, cisplatin, or irradiation. Suppression of tumor growth by OBP-301 (Fig. 5A) was accompanied by a significant decrease in *CD133* mRNA at 2 weeks after the final treatment (Fig. 5B). In contrast, although cisplatin and radiation also suppressed tumor growth to a similar extent as OBP-301 (Fig. 5A), cisplatin did not affect, and radiation significantly increased *CD133* mRNA expression at 1 week after the final treatment (Fig. 5B). Immunohistochemistry of CD133-stained tumor sections also showed that OBP-301 reduced the frequency of $CD133^+$ cells, whereas cisplatin and irradiation increased the frequency compared with control (Fig. 5B).

Next, we visualized treatment dynamics in established FUCCI-expressing MKN45 tumor xenografts with or without OBP-301 infection (Supplementary Fig. S10B). FUCCI-expressing MKN45 tumors had a distribution of cancer cells in G_0–G_1, S, and G_2–M phases (Fig. 5A). As tumors grew bigger, cancer cells in G_0–G_1 phase increased (Fig. 5C and D), indicating the existence of dormant cancer cells.